Phonon scattering at kinks in suspended graphene

Dolleman, Robin Joey; Blanter, Yaroslav; van der Zant, Herre; Steeneken, Peter; Verbiest, Gerard

DOI
10.1103/PhysRevB.101.115411

Publication date
2020

Document Version
Final published version

Published in
Physical Review B

Citation (APA)
Dolleman, R. J., Blanter, Y., van der Zant, H., Steeneken, P., & Verbiest, G. (2020). Phonon scattering at kinks in suspended graphene. *Physical Review B*, *101*(11), Article 115411. https://doi.org/10.1103/PhysRevB.101.115411

PHYSICAL REVIEW B **101**, 115411 (2020)

Phonon scattering at kinks in suspended graphene

Robin J. Dolleman,[1,*] Yaroslav M. Blanter,[1] Herre S. J. van der Zant,[1] Peter G. Steeneken,[1,2] and Gerard J. Verbiest[2,†]
[1]*Kavli Institute of Nanoscience, Delft University of Technology, Lorentzweg 1, 2628 CJ, Delft, The Netherlands*
[2]*Department of Precision and Microsystems Engineering, Delft University of Technology, Mekelweg 2, 2628 CD, Delft, The Netherlands*

(Received 25 September 2019; revised manuscript received 8 January 2020; accepted 19 February 2020; published 11 March 2020)

Recent experiments have shown surprisingly large thermal time constants in suspended graphene ranging from 10 to 100 ns in drums with a diameter ranging from 2 to 7 μm. The large time constants and their scaling with diameter points toward a thermal resistance at the edge of the drum. However, an explanation of the microscopic origin of this resistance is lacking. Here, we show how phonon scattering at a kink in the graphene, e.g., formed by sidewall adhesion at the edge of the suspended membrane, can cause a large thermal time constant. This kink strongly limits the fraction of flexural phonons that cross the suspended graphene edge, which causes a thermal resistance at its boundary. Our model predicts thermal time constants that are of the same order of magnitude as experimental data and shows a similar dependence on the circumference. Furthermore, the model predicts the relative in-plane and out-of-plane phonon contributions to graphene's thermal expansion force, in agreement with experiments. We thus show an unconventional thermal boundary resistance which occurs solely due to strong deformations within a two-dimensional material.

DOI: 10.1103/PhysRevB.101.115411

I. INTRODUCTION

The transport of phonons and heat in two-dimensional (2D) materials like graphene [1] is essentially different from that in three-dimensional (3D) materials, due to their large anisotropy between the in-plane and out-of-plane stiffness. This leads to extraordinary thermal properties that have attracted much interest [2–14]. Recently, we demonstrated a thermomechanical method [15] to characterize the thermal time constant τ of suspended graphene membranes. We found that the values of τ are considerably larger than expected. Moreover, τ was found to scale with the diameter of the suspended drums, which could be explained by a model in which the transient heat transport is limited by a thermal boundary resistance. Several studies have shown that such a thermal resistance can emerge within the graphene due to grain boundaries [16,17], carbon isotope doping [18], encasing with boron nitride [19], a step in the substrate [20], or a change in the number of graphene layers [21]. However, none of these microscopic models predict the emergence of a sufficiently large thermal boundary resistance to account for the large thermal time constants observed in Ref. [15].

Here, we theoretically analyze phonon transport in suspended graphene membranes and compare this to experimental works [15,22] on devices as depicted in Fig. 1, to explain the large values of the thermal time constants. A laser heats up the center of the membrane, and the resulting heat is transported by lattice vibrations (phonons) to the substrate. It is often observed that suspended 2D materials show a kink at their edge due to sidewall adhesion [23–25], which is the case we will examine in this work. For phonons to leave the suspended membrane, they have to be transmitted across the kink between the suspended and supported graphene. We show that this transmission is very small for flexural phonons, which is related to their low propagation speed compared to the in-plane phonons. Consequently, a thermal resistance can arise in 2D materials from a kink within the material itself. The model predicts thermal time constants τ_{ZA} in line with the experimental values found in Ref. [15].

The remainder of this article is structured as follows: Sec. II constructs the mechanical model to calculate the transmission and reflection coefficients of a phonon incident on a kink. In Sec. III, we use the mechanical modal as a boundary condition to construct a two-temperature model from which the thermal time constants and their relation to the thermal expansion forces can be calculated. In Sec. IV, we discuss how the model could be improved and make suggestions for future experiments. Finally, the conclusions are presented in Sec. V.

II. MECHANICAL MODEL FOR A KINK

To examine the effect of kinks in graphene on phonon transport, we develop a mechanical model that evaluates the phonon scattering at a kink with an angle β and gives the phonon transmission and reflection probabilities. Figure 2 shows that after an acoustic phonon reaches the kink, it will be converted in a combination of reflected and transmitted longitudinal (LA), transverse (TA), and flexural (ZA) acoustic phonons. We find the transmission and reflection coefficients for each incident phonon mode by solving six coupled equations: three from the continuity of displacement and three from the continuity of stress. The derivation follows the method by Kolsky [26] closely, with additions to include

---

[*] Present address: Second Institute of Physics, RWTH Aachen University, 52074 Aachen, Germany; R.J.Dolleman@tudelft.nl

[†] G.J.Verbiest@tudelft.nl

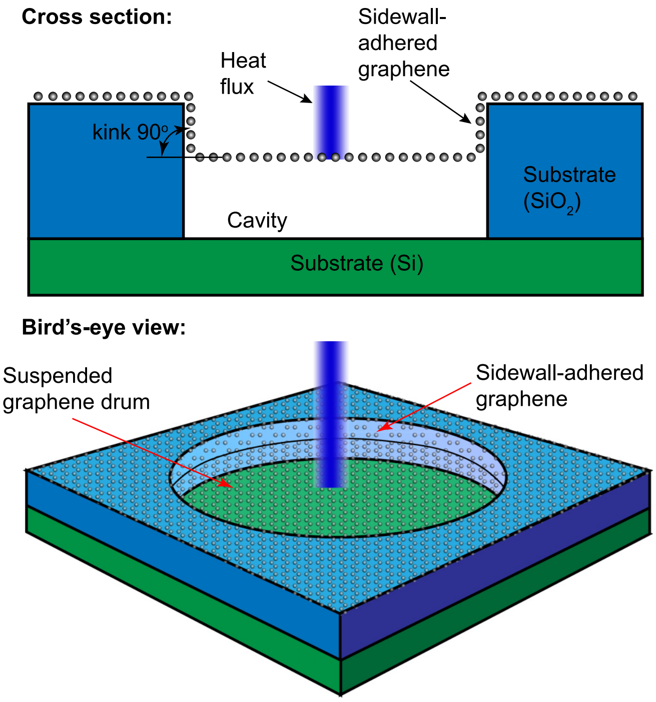

FIG. 1. Model system under consideration in this work. A graphene drum is suspended over a cavity and adheres to the sidewall, introducing a kink at the edge of suspended graphene. The suspended graphene is heated by a laser and heat flow in the suspended graphene is studied.

the effects of the flexural phonons. To simplify the analysis, the second kink between the supported and sidewall-adhered graphene is not taken into account and all of the supported graphene and the substrate is assumed to be an ideal heat sink. In order to only observe the geometry-induced effects of the kink, we set the elasticity parameters and tension equal in both domains, resulting in equal propagation velocities for each phonon mode on the suspended and supported graphene.

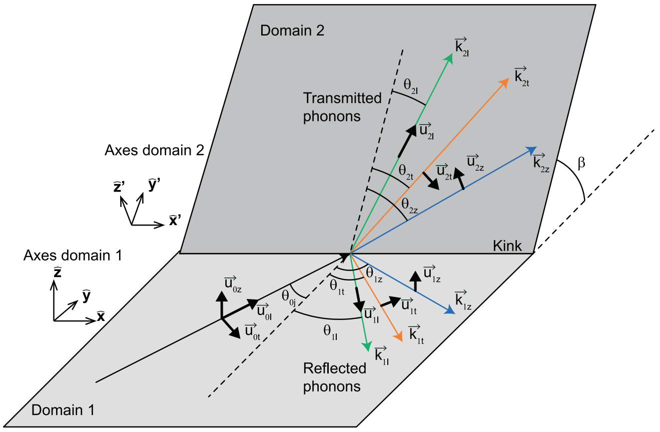

FIG. 2. Phonon scattering on a kink with angle β in graphene. A phonon with amplitude u_{0j} is incident on the kink with an angle θ_{0j}, and the sharp kink in the graphene has an angle β. The incident phonon can scatter into six possibilities, either transmission at LA, TA, or ZA phonon or reflection as a LA, TA, or ZA phonon.

A. Snell's law

The model calculates the transmission coefficients $w_{ij\rightarrow qr}$, which represent the fraction of phonons in mode j on domain i that reach the kink and end up into phonon mode r on domain q. Here, we use $j, r = l, t, z$ for LA, TA and ZA phonon, respectively, and $i, q = 1, 2$ for suspended and supported graphene, respectively. Also, the subscript $i = 0$ is used to indicate an incident phonon from domain 1. We consider the reflection and transmission of an incident phonon with amplitude $\vec{u}_{0j}$ and with an incident angle θ_{0j} (Fig. 2) that is incident on an interface where the graphene has a kink with angle β. If the phonon propagation speed c_{ij} is known, we can find the angles of reflection and refraction with respect to the normal using Snell's law:

$$\sin\theta_{ij} = \frac{c_{ij}}{c_{0j}} \sin\theta_{0j}. \tag{1}$$

With the angles of refraction known, only the amplitudes $\vec{u}_{ij}$ of the reflected and refracted waves are unknown. To find these, we construct six coupled equations in the following subsections.

B. Continuity of deflection

The mechanical motion $\vec{q}_{ij}$ around the static position of the membranes is described by a wave with amplitude $\vec{u}_{ij}$:

$$\vec{q}_{ij}(x, y, t) = \vec{u}_{ij}\cos(\omega t + k_x x + k_y y), \tag{2}$$

where k_x is the component of the wave vector $\vec{k}$ in the x direction of the local axis and k_y in the y direction. Positive directions of the displacements and wave vectors are defined as drawn in Fig. 2. The displacements in domain 2 are projected onto the coordinate system of domain 1, which gives three expressions for the continuity of displacement at the kink:

$$\sum_j \vec{q}_{1j} = \sum_j \vec{q}_{2j}, \tag{3}$$

By substituting Eq. (2) in Eq. (3) and setting the origin $x = y = z = t = 0$ to the location and time where the phonon hits the kink, one obtains expressions that only depend on the amplitudes $\vec{u}_{ij}$ and the angles θ_{ij} and β. The full expressions are presented in the Supplemental Material [27].

C. Continuity of stress

The continuity of stress implies that the total tension is equal on both sides of the kink. Figure 3 shows the relevant tension components, where $n_{ij,yy}$ and $n_{ij,zz}$ are the tension components in the $\hat{\mathbf{y}}$, $\hat{\mathbf{z}}$ directions, respectively, and $n_{ij,xy}$ is the shear stress component. Note that $n_{ij,xx}$ does not play a role in the transmission of elastic waves because of rotational symmetry along the $\hat{\mathbf{x}}$ direction. Furthermore, the components $n_{ij,xz} = n_{ij,yz} = 0$ due to the two-dimensional nature of the material. Each remaining tension component of the tension tensor n is then split into a static part $\overline{n}$ and a dynamic part δn [for example, $n_{ij,yy}(t) = \overline{n}_{i,yy} + \delta n_{ij,yy}(t)$; the static component cannot be attributed to a specific phonon mode and therefore the subscript j is omitted]. To formulate the continuity of stress equations, we only take the dynamic stress

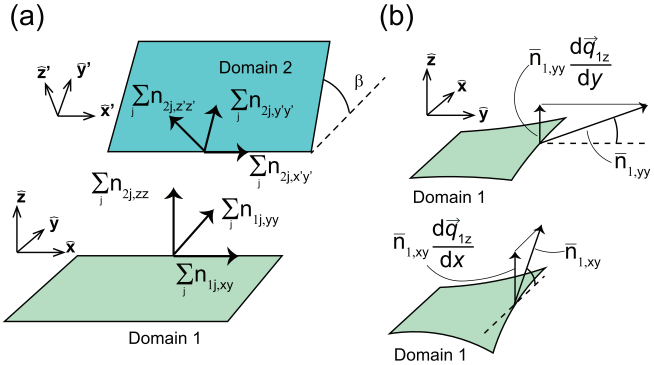

FIG. 3. Cross section of the membrane showing the stresses at the kink. (a) The three stress components at the interface between both domains, which are added together in the axes of domain 1 to obtain the continuity of stress equations. (b) The out-of-plane displacement of the membrane $\vec{q}_{iz}$ results in a out-of-plane projection of the in-plane stress and shear components.

components into account, since the equilibrium is already satisfied for the static part of the stress.

The dynamic stress components $\delta n_{ij,yy}$ and $\delta n_{ij,xy}$ are related to the deflection-induced dilatation and shear of the lattice by the relations [26]:

$$\delta n_{ij,yy} = (\lambda + 2\mu)\frac{d\vec{q}_{ij}}{dy}\hat{\mathbf{y}} + \lambda\frac{d\vec{q}_{ij}}{dx}\hat{\mathbf{x}}, \tag{4}$$

$$\delta n_{ij,xy} = \mu\frac{d\vec{q}_{ij}}{dy}\hat{\mathbf{x}} + \mu\frac{d\vec{q}_{ij}}{dx}\hat{\mathbf{y}}, \tag{5}$$

where λ and μ are the Lame parameters; note that these components are expressed in the local axes of each domain. The dynamic component $\delta n_{iz,zz}$ is a result of the flexural phonons, whose out-of-plane motion allows the static in-plane stress components $\bar{n}_{i,yy}$ and $\bar{n}_{i,xy}$ to be rotated into the $\hat{\mathbf{z}}$ direction of the local axes, as shown in Fig. 3(b). The out-of-plane deflections $\vec{q}_{iz}$ are assumed to be small enough to not introduce significant dynamic tension modulations due to elastic deformation compared to the static pretension. This gives for the tension modulation component $\delta n_{iz,zz}$ in the local axis of each domain:

$$\delta n_{iz,zz} = \bar{n}_{i,yy}\frac{d\vec{q}_{iz}}{dy}\hat{\mathbf{y}} + \bar{n}_{i,xy}\frac{d\vec{q}_{iz}}{dx}\hat{\mathbf{x}}. \tag{6}$$

By substituting Eq. (2) into Eqs. (4)–(6), the stress components shown in Fig. 3 can be calculated and projected onto each of the axes of domain 1:

$$\sum_{\alpha\zeta}\sum_{j}\delta n_{ij,\alpha\zeta}\hat{\mathbf{s}}_{\gamma} = \sum_{\alpha\zeta}\sum_{j}\delta n_{ij,\alpha\zeta}\hat{\mathbf{s}}_{\gamma}, \tag{7}$$

where $\alpha\zeta \in \{xy, yy, zz, x'y', y'y', z'z'\}$, $\gamma \in \{x, y, z\}$ and $\hat{\mathbf{s}}_{\gamma}$ is a unit vector pointing in one of the directions of domain 1. This results in three expressions that only depend on $\vec{u}_{ij}$, θ_{ij}, β and the pretension components $\bar{n}$, which are shown in the Supplemental Material [27].

D. Integrated transmission coefficients

The six equations we derived [Eqs. (3) and (7)] can be solved simultaneously for each incident mode, by setting $|u_{0j}| = 1$ (see the Supplemental Material for more details [27]). From the amplitudes of the transmitted and reflected waves, one can calculate the energy flux of each wave leaving the kink [$B_{ij} = \rho\omega^2 c_{ij}|u_{ij}|^2\mathrm{Re}(\cos\theta_{ij})$, where ρ is the density of graphene and ω is the phonon frequency] and from that define the transmission coefficient as [28]

$$w_{0j\to qr}(\theta_{0j}) = \frac{B_{qr}}{B_{0j}} = \frac{c_{qr}|u_{qr}|^2\mathrm{Re}(\cos\theta_{qr})}{c_{0j}|u_{0j}|^2\cos\theta_{0j}}, \tag{8}$$

where the incoming wave amplitude $|u_{0j}| = 1$. Note that the density ρ drops out of the equation because it is equal on both domains. In the model, $w_{0j\to qr}(\theta_{0j})$ is integrated over all incoming angles θ_{0j} to obtain the total transmission or reflection coefficient of each scattering process $\bar{w}_{0j\to qr}$. $\bar{w}_{0j\to qr}$ can then be used to calculate the total heat flux crossing the boundary. However, we first study the angular-dependence of $w_{0j\to qr}$ below.

E. Transmission probabilities as function of incident angle for $\beta = 90°$

Figure 4 shows the angle-dependent transmission coefficients $w_{0j\to qr}(\theta_0)$ of all the three phonon modes on a graphene membrane with a pretension of $\bar{n}_{1,xx} = \bar{n}_{1,yy} = \bar{n}_{2,xx} = \bar{n}_{2,yy} = 0.03$ N/m (based on estimates from Ref. [15]), $\bar{n}_{1,xy} = \bar{n}_{2,xy} = 0$ N/m, and $\beta = 90°$. The Lame parameters $\lambda = 15.55$ J/m^2 and $\mu = 103.89$ J/m^2 are taken from the literature [29].

The transmission of incident LA phonons is mostly affected with respect to $\beta = 0°$ at small incident angles. This is because when $\theta_{0j} = 0°$, $\vec{u}_{0l} \parallel \vec{u_{2z}}$, as shown in the inset of Fig. 4(a). The continuity of deflection then enforces that LA phonons can only transmit into ZA phonons, which are significantly mismatched in propagation speed c_{ij} [$c_{il} = \sqrt{(\lambda_i + 2\mu_i)/\rho h_g} = 17.0$ km/s, $c_{it} = \sqrt{\mu/\rho h_g} = 11.6$ km/s, and $c_{iz} = \sqrt{\bar{n}/\rho h_g} = 0.2$ km/s, where $h_g = 0.335$ nm is the thickness of graphene]. Using acoustic impedance mismatch theory [30], we obtain a transmission coefficient of $4c_{2z}c_{1l}/(c_{2z} + c_{1l})^2 = 0.046$, matching the value obtained by the model for $\theta_0 = 0°$. At larger incident angles, efficient transmission into LA and TA phonons becomes possible, raising the total transmission coefficient.

As shown in Fig. 4(b), incident TA phonons can fully transmit at small incident angles. This can also be understood from the continuity of displacement: Since the amplitudes $\vec{u}_{0t} \parallel \vec{u_{2t}}$ [see inset in Fig. 4(b)], incident TA phonons with $\theta_0 = 0$ can only transmit as TA phonons, meaning that there is no change in propagation speed and acoustic impedance. At an incident angle $\theta_0 = 43°$, a sharp feature is observed. This corresponds to the critical angle $\theta^* = \arcsin c_{it}/c_{il}$, where from Eq. (1) the angle of refraction into LA phonons would exceed 90°, meaning that TA phonons can no longer be transmitted or reflected into LA phonons.

The incoming ZA phonons in Fig. 4(c) (note the horizontal axis scale) show a remarkably low transmission, due to the large propagation speed differences between in-plane and out-of-plane phonons. At very small incident angles, at an incoming angle $\theta_{0z} = 0°$: $\vec{u}_{0z} \parallel \vec{u}_{2l}$. Since the change in acoustic impedance is the same as in the case for an incoming LA phonon at $\theta_{0l} = 0°$, the transmission probability (0.046)

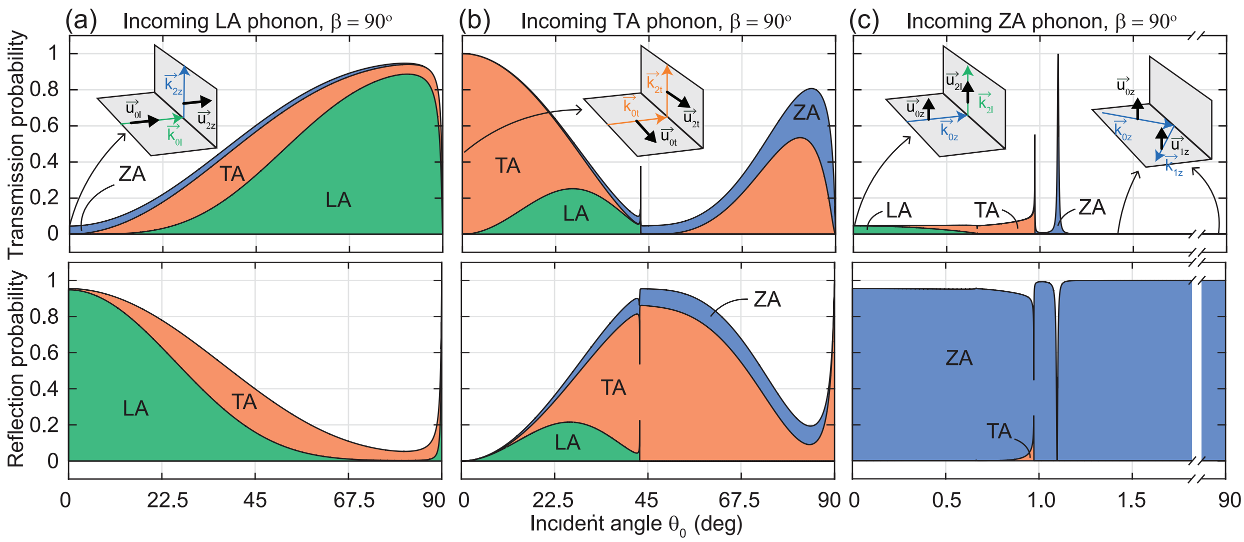

FIG. 4. Transmission and reflection probabilities $w_{ij\to qr}(\theta_0)$ as function of incident angle θ_0 for (a) LA, (b) TA, and (c) ZA phonons. The insets show a sketch of the incident and transmitted phonons when $\theta_0 = 0°$, and the additional inset in panel (c) shows the total internal reflection of the ZA phonons. Note the different x axis in the case of Fig. (c), enlarging the low-angle behavior.

is equal. The low speed of the flexural phonons compared to the in-plane phonons results in small critical angles, the largest being $\theta^* = \arcsin c_{iz}/c_{it} = 0.99°$. Above this angle, the flexural phonons can no longer reflect or transmit as LA or TA phonons, and ZA phonons are generally not transmitted. Because of this, the integrated transmission coefficient of ZA phonons is three orders of magnitude smaller than those of the in-plane phonons. A striking phenomenon is the transmission peak near $\theta_0 = 1.1°$, which emerges due to a resonant excitation of waves residing at the kink. This effect resembles the formation of Rayleigh waves on the surface of the solid material interfacing with a liquid [28]. Furthermore, similar interface waves have been observed between two graphene domains in semimolecular dynamics simulations [31].

III. TWO-TEMPERATURE MODEL

The goal of this section is to demonstrate that the presented model is in line with the large values of thermal time constants found in Ref. [15] and the observation of the opposing thermal expansion forces in Ref. [22]. We analyze the situation where an (optothermal) heat flux is incident at the center of a circular drum. In the case of local thermal equilibrium (where all the acoustic phonon modes have the same temperature), the boundary scattering effect presented above cannot account for the experimental observations, due to the high transmission coefficients of the in-plane phonons (see the Supplemental Material [27]). Therefore, we construct a two-temperature model to describe heat transport through suspended graphene, where the in-plane LA and TA phonons are assumed to be at a different temperature than the out-of-plane flexural ZA phonons. It is assumed that the heat generates only in-plane acoustic phonons due to selective electron-phonon coupling [32,33], which propagate outward from the center. Conversion between in-plane and out-of-plane phonon modes on the suspended part of the drum is neglected due to their weak mutual interactions [34]. At the edge of the drum, the phonons are transmitted and reflected by the kink in graphene. Because of this reflection, a conversion between different phonon modes can occur that can be analyzed by the theory from the previous section.

Thus, we can determine the time-dependent internal energies of different phonon modes on the suspended part of the graphene drum. Transmitted phonons are lost, but ZA phonons can be reflected multiple times at the edge of the graphene, which leads to a significantly larger value of τ_{ZA}, as found in experiments. Because of the different transmission coefficients for ZA and in-plane phonons, large differences in the phonon densities, and related phonon bath temperatures of the different phonon modes, can occur. As a result of this, local thermal equilibrium is violated, similar to recent predictions of Vallabhaneni *et al.* [33]. To model this, we construct a similar two-temperature model where scattering between in-plane and out-of-plane phonon modes is neglected. Instead of this, the phonon conversions at the kink are taken into account.

To simplify the problem we note that, according to Fig. 4, the in-plane phonons have a high probability of crossing the kink at the edge of the suspended graphene and therefore experience a low thermal resistance. The flexural ZA phonons, on the other hand, are confined to the drum due to total internal reflection and therefore experience a large thermal resistance, making them responsible for the long thermal time constants τ_{ZA} observed in experiments. To predict the long thermal time constant τ_{ZA}, this means that analysis can be simplified by initially focusing on the flexural phonons alone and explain the value of the thermal time constants observed in Ref. [15] (Subsec. III A). After this, the model will be expanded to also include the flow of heat attributed to the in-plane acoustic phonons, to explain the opposing thermal expansion forces in Ref. [22] (Subsecs. III B–III E). The final subsection, Subsec. III F, estimates the value of the thermal time constant of the in-plane acoustic phonons, to verify that it is much shorter than that of the flexural acoustic phonons.

A. Time constant for flexural phonons

In this section, we study a simplified model that predicts the time constant τ_{ZA}, that is compared to experimental values [15,22] of the time constant. This comparison allows us to estimate the average pretension $\bar{n}$ in the membrane, which will be used in the following subsection. Assuming the environmental temperature is higher than the Debye temperature for ZA phonons, expressions for the heat capacity $\mathcal{C}_{\mathrm{ZA}}$ and thermal resistance $\mathcal{R}_{\mathrm{ZA}}$ for a circular membrane were derived in Ref. [15]:

$$\mathcal{R}_{\mathrm{ZA}} = \frac{1}{G_{B,z} h_g 2\pi a} = \frac{A_{uc}}{2\pi a k_B \sum_r \bar{w}_{1z\to 2r} c_{\mathrm{ZA}}}, \tag{9}$$

$$\mathcal{C}_{\mathrm{ZA}} = c_{p,z} \rho h_g \pi a^2 = \frac{k_B \pi a^2}{A_{uc}}, \tag{10}$$

where $G_{B,z}$ is the thermal boundary conductance of the ZA phonons, h_g is the thickness of graphene, a is the drum radius, k_B is the Boltzmann constant, c_{ZA} is the propagation speed of ZA phonons, and A_{uc} is the unit cell area of graphene. For a circular membrane, the flexural phonon time constant $\tau_{\mathrm{ZA}} = \mathcal{R}_{\mathrm{ZA}}\mathcal{C}_{\mathrm{ZA}}$ is described by the equation

$$\tau_{\mathrm{ZA}} = \frac{a}{2\sum_r \bar{w}_{1z\to 2r} c_{\mathrm{ZA}}}, \tag{11}$$

Figure 5 shows the transmission coefficient and time constant τ_{ZA} as a function of kink angle β and for different values of the average pretension $\bar{n}$. Since the phonon velocities on the supported and suspended graphene are equal by assumption, the transmission coefficient of the ZA phonons is equal to 1 when the kink angle is 0 or 180 deg. The transmission coefficient already changes dramatically for small kink angles. The transmission coefficient is minimal for a kink of 90 deg.

We compare the model to the experimental values of τ/a found in related works [15,22]. In Fig. 5(b), the gray area indicates the highest and lowest observed value of τ/a and the dashed line indicates the mean value $\overline{\tau/a} = 0.029$ s/m. Assuming sidewall adhesion with a kink angle of 90 deg, we estimate the phonon speed to be 1.0 km/s on average, corresponding to a tension of ≈0.8 N/m. This value is reasonable compared to pretension values obtained in literature [35], and we will use this value in the following subsections.

B. Model for opposing thermal expansion forces

In this subsection, we calculate the ratio between the opposing thermal expansion forces in the steady-state regime, which are found in experiments in Ref. [22]. As explained above and in the Supplemental Material [27], we expect the in-plane and flexural acoustic phonons to be at different temperatures and therefore require a two-temperature model to describe heat transport in the suspended graphene. To do this, we assume that the LA and TA phonons are always in local thermal equilibrium with each other. This is supported by the results of Vallabhaneni *et al.* [33], who also analyzed suspended graphene heated by a laser, and found the LA and TA phonons to be at the same temperature. The internal energies are related to the modal temperatures by the expression [15]

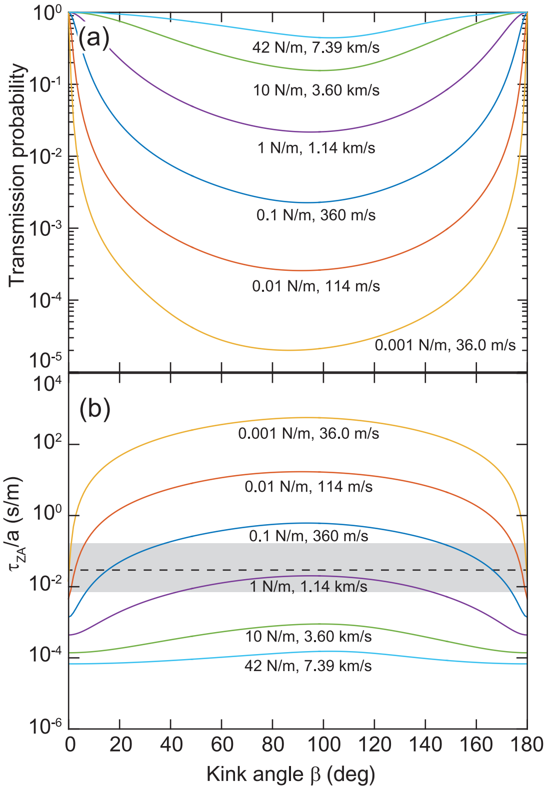

FIG. 5. (a) Fraction of transmitted flexural phonons $\sum_r \bar{w}_{1z\to 2r}$ for different values of the pretension as a function of kink angle β. (b) Time constant attributed to the flexural acoustic phonons τ_{ZA} divided by drum radius a as a function of kink angle β. The pretension is varied to show the effect of phonon propagation speed on the time constant. The gray area indicates the experimental range from Ref. [22] and the dashed line shows the experimental mean.

$$\begin{aligned} U_{ij} &= \frac{\zeta(3) k_B^3 T_{\mathrm{LA+TA}}^3}{\pi c_{ij}^2 \hbar^2 h_g} \quad \text{for } j = t, l, \\ U_{ij} &= \frac{k_B T_{\mathrm{ZA}}}{h_g A_{uc}} \quad \text{for } j = z, \end{aligned} \tag{12}$$

where $\hbar$ is the reduced Planck constant and $\zeta(3) \approx 1.21$ Apéry's constant. Using Eq. (12), the internal energy of the LA phonons U_{1l} is related to the internal energy of the TA phonons U_{1t} by

$$U_{1t} = \frac{c_{1l}^2}{c_{1t}^2} U_{1l}. \tag{13}$$

Because of the selective electron-phonon coupling, the LA and TA phonon modes are also the only modes that will receive the heat flux from the laser [32,33]. For the ZA phonon bath, we assume that the heat transport is limited by the boundary resistance induced by the kink, as this was also used to calculate τ_{ZA} in Subsec. III A above.

Using the assumptions above, we use the heat equation in cylindrical coordinates [4,9] to find the change in internal energy of the in-plane phonons ΔU_{1l}:

$$\frac{\kappa_{\mathrm{LA+TA}}}{\rho c_{p,\mathrm{LA+TA}}}\frac{1}{r}\frac{d}{dr}\left(r\frac{d\Delta U_{1l}}{dr}\right)+Q'''=0, \tag{14}$$

where $\kappa_{\mathrm{LA+TA}}$ is the thermal conductivity of the in-plane phonon bath, $c_{p,\mathrm{LA+TA}}$ is the specific heat of the in-plane phonon bath, and Q''' is the volumetric heat flux of the laser. This is described by the Gaussian spatial dependence:

$$Q'''=Q_0\exp\left(\frac{-r^2}{r_0^2}\right), \tag{15}$$

where r_0 is the radius of the laser spot, estimated to be $r_0 =$ 285 nm. Using this spatial dependence, the general solution to Eq. (14) is

$$U_{\mathrm{LA}}(r)=A_1+A_2\ln(r)+A_3\mathrm{Ei}\left(\frac{-r^2}{r_0^2}\right), \tag{16}$$

where A_1, A_2, and A_3 are constants to be determined and Ei is the exponential integral function. A_1, A_2, and A_3 are found by enforcing a continuous solution when $r \rightarrow 0$ and applying an energy balance at the boundary of the drum. ΔU_{1z} is modeled by assuming that the thermal resistance at the edge of the drum is limiting the heat transport; therefore, ΔU_{1z} is uniform over the suspended drum. Since ΔU_{1z} appears in the boundary conditions, solving Eq. (16) results in solutions for $\Delta U_{1l}(r)$ and ΔU_{1z} which are presented in the Supplemental Material [27].

The force that actuates the out-of-plane motion of the membrane is proportional to the strain in the membrane [36]. To find the ratio between the thermal expansion forces, one can therefore convert the internal energies to the mechanical strain contribution from each phonon mode $\Delta\epsilon_j$ using the expression [37]

$$\Delta\epsilon_j=-\frac{1}{4K}\gamma_j U_j, \tag{17}$$

where $K = 158$ GPa the bulk modulus. The ratio between the thermal expansion forces $C_{\mathrm{LA+TA}}/C_{\mathrm{ZA}} = (\Delta\epsilon_{\mathrm{LA}} + \Delta\epsilon_{\mathrm{TA}})/\Delta\epsilon_{\mathrm{ZA}}$ becomes

$$\frac{C_{\mathrm{LA+TA}}}{C_{\mathrm{ZA}}}=\frac{\gamma_{\mathrm{LA}}\Delta\bar{U}_{1l}+\gamma_{\mathrm{TA}}\frac{c_{1l}^2}{c_{1t}^2}\Delta\bar{U}_{1l}}{\gamma_{\mathrm{ZA}}\Delta U_{1z}}, \tag{18}$$

where $\bar{U}_{1l}$ is the average internal energy of the LA phonons over the surface of the drum. This ratio of the forces determines the mechanical out-of-plane response of the membrane, and should therefore match the force ratio observed in experiments [22].

Evaluation of the model requires several parameters from theory. First, the in-plane thermal conductivity $k_{\mathrm{LA+TA}}$ is required, whose value can show considerable spread in literature [8,34,38]. Second is the mode Grüneisen parameter γ_{ZA}, which is difficult to calculate at low phonon frequencies [39–41]. Here, we use literature values of the mode Grüneisen parameters: $\gamma_{\mathrm{LA}} = 1.06$, $\gamma_{\mathrm{TA}} = 0.40$, and $\gamma_{\mathrm{ZA}} = -4.17$ from Mann *et al.* [41]. Finally, the angular distribution of θ_{0j} at which phonons are incident at the boundary is of influence. For now, we assume a uniform angular distribution, but its influence will be investigated further below.

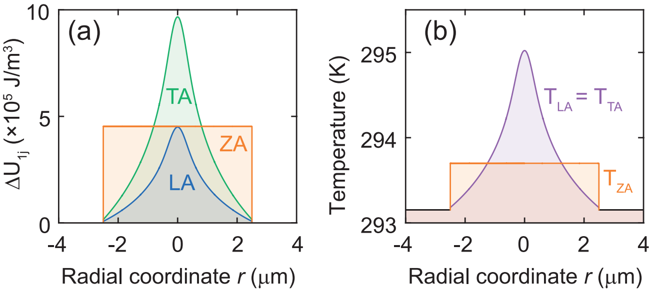

FIG. 6. (a) Change in internal energy and (b) modal temperature as a function of radial coordinate r with in-plane thermal conductivity $\kappa_{\mathrm{LA+TA}} = 2000$ W/m K [42], laser spot size $r_0 = 285$ nm, drum radius $a = 2.5$ μm and total absorbed laser power $Q_{\mathrm{laser}} = 1$ μW.

C. Modal temperatures

First, we study the internal energy and modal temperature in the membrane as a function of position. As a starting point, we take the in-plane thermal conductivity of graphite as $\kappa_{\mathrm{LA+TA}}$, which is taken to be 2000 W/m K [42]. The internal energy as a function of position r is shown in Fig. 6(a). These values are converted to temperature in Fig. 6(b) by using Eq. (12). The ZA phonons show a large temperature jump due to their large thermal boundary resistance. Since the rate of ZA phonon generation from the in-plane phonon bath is much higher than that of ZA phonons leaving the membrane, this phonon bath reaches relatively high internal energies, even though this bath only receives a small fraction of the total heat flux supplied to the system due to selective electron-phonon coupling. Converting the average internal energies to the force ratio [Eq. (18)], we find for this specific drum diameter of 5 μm and $\kappa_{\mathrm{LA+TA}} = 2000$ W/m K that $-C_{\mathrm{LA+TA}}/C_{\mathrm{ZA}} = 0.098$. Compared to experiments, the median value of $-C_{\mathrm{LA+TA}}/C_{\mathrm{ZA}} = 0.2$ for a 5-μm diameter drum, the model thus predicts values of the force ratio in the right order of magnitude.

If the ratio $-C_{\mathrm{LA+TA}}/C_{\mathrm{ZA}}$ is calculated as a function of diameter, however, the model predicts an increasing trend, while the experiments show a decreasing trend (Fig. 7). Likely this is due to the assumption that $\kappa_{\mathrm{LA+TA}}$ is constant as a

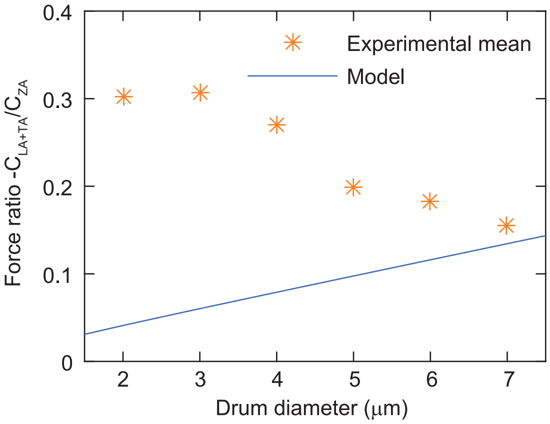

FIG. 7. $-C_{\mathrm{LA+TA}}/C_{\mathrm{ZA}}$ as a function of drum diameter calculated from Eq. (18) compared to experimental mean values from Ref. [22]. A constant value of $\kappa_{\mathrm{LA+TA}} = 2000$ W/m K and $r_0 = 285$ nm is assumed.

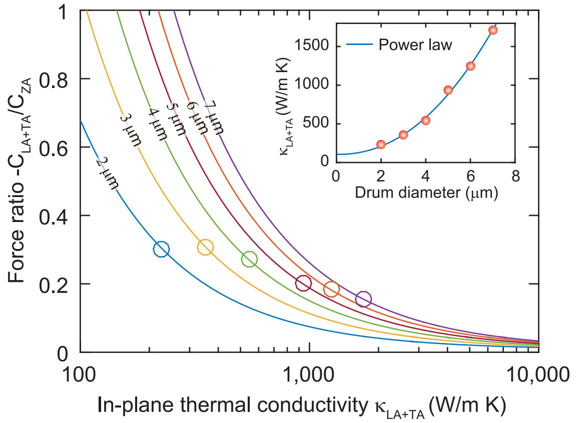

FIG. 8. Dependence of $-C_{\mathrm{LA+TA}}/C_{\mathrm{ZA}}$ on the thermal conductivity of the in-plane phonons plotted for different drum diameters, using the model in Sec. III B. The circles represent the experimental mean from Ref. [22]. The inset shows the extracted in-plane thermal conductivity as a function of drum diameter based on the experimental mean of $-C_{\mathrm{LA+TA}}/C_{\mathrm{ZA}}$, with a power law ($\kappa_{\mathrm{LA+TA}} = c_0 + c_1(2a)^p$) fit to the data.

function of diameter, while literature suggests that the effective thermal conductivity $\kappa_{\mathrm{LA+TA}}$ is length dependent [8,34,38]. This is because the mean free path of the in-plane phonons is not small enough compared to the drum size and, as a consequence, the phonon transport is still partly ballistic [43,44]. This causes boundary effects to have an important affect on the in-plane thermal conductivity $\kappa_{\mathrm{LA+TA}}$. In Subsec. III D, we will investigate whether a diameter-dependent $\kappa_{\mathrm{LA+TA}}$ can account for the experimental results.

Another consequence of the (partly) ballistic nature of the phonon transport is that the angular distribution of the phonons incident on the boundary is no longer uniform. Keeping in mind that phonons are primarily generated in the center of the drum and initially propagate radially outward, small drums have more phonons with normal incidence on the boundary. On the other hand, large drums have a more uniform distribution, as more scattering events are expected to occur between the center and the edge of the drum. As shown in Fig. 4, the transmission of phonons is strongly dependent on their incident angle, and this could account for the anomalous diameter dependence of $-C_{\mathrm{LA+TA}}/C_{\mathrm{ZA}}$ observed in the experiments. Therefore, the influence of the angular distribution of incident phonons is investigated in Subsec. III E.

D. Influence of the in-plane thermal conductivity

To explain the diameter dependence of the ratio $-C_{\mathrm{LA+TA}}/C_{\mathrm{ZA}}$ in Ref. [22], we first study the effect of the thermal conductivity of the in-plane phonons $\kappa_{\mathrm{LA+TA}}$. Figure 8 shows the calculated ratio $-C_{\mathrm{LA+TA}}/C_{\mathrm{ZA}}$ as a function of $\kappa_{\mathrm{LA+TA}}$ for different drum diameters. As the thermal conductivity of the in-plane phonons increases, the ratio $-C_{\mathrm{LA+TA}}/C_{\mathrm{ZA}}$ decreases. This is because the in-plane phonons reach a lower temperature, which reduces the amplitude $C_{\mathrm{LA+TA}}$. Using the experimental mean of $-C_{\mathrm{LA+TA}}/C_{\mathrm{ZA}}$, the in-plane thermal conductivity needed to match theory and experiment can be extracted as shown in the inset in Fig. 8. A strong increase in thermal conductivity is observed as the drum diameter increases. An increase of in-plane thermal conductivity with increasing diameter has been reported in various works [8,34,38,45,46]. However, if we fit a power law to $\kappa_{\mathrm{LA+TA}} = c_0 + c_1(2a)^p$ (see inset of Fig. 8), we find an exponent $p = 2$. In the literature, a much weaker logarithmic divergence of $\kappa_{\mathrm{LA+TA}}$ with length is reported [34,38,45,46]. Furthermore, a divergence that is stronger than $\kappa_{\mathrm{LA+TA}} \propto a$ would exceed that of a ballistic 1D harmonic lattice without phonon scattering [47]. Therefore, the obtained exponent $p = 2$ is unlikely to be real, which suggests that other effects should be taken into consideration to explain the diameter dependence of $-C_{\mathrm{LA+TA}}/C_{\mathrm{ZA}}$.

E. Influence of angular phonon distribution

So far, we have assumed the incoming angular distribution of the phonons to be uniform. However, since the mean free path of the phonons is not necessarily much shorter than the size of the suspended membrane [32,43,44], a nonuniform angular distribution is expected. Therefore, in this section, we alter the incoming phonon distribution with a distribution function $f(\theta_0)$, to analyze the influence of a nonuniform angular distribution on the ratio $-C_{\mathrm{LA+TA}}/C_{\mathrm{ZA}}$, using the model in Sec. III B. We adapt the integration of the transmission probabilities to include $f(\theta_0)$, which is the normalized incident phonon distribution:

$$\bar{w}_{ij\to qr} = \frac{2}{\pi}\int_0^{\pi/2} f(\theta_0)w_{ij\to qr}(\theta_0)d\theta_0. \tag{19}$$

We simplify the analysis by only taking into account variations in $f(\theta_0)$ for the LA and TA phonons, since this is the bath where phonons are primarily generated. The heat flows consecutively into the ZA phonons and this phonon bath experiences many collisions at the boundary; therefore, this angular distribution is assumed to be uniform. The incoming phonon distribution of the LA and TA phonons is altered by the following step function:

$$f(\theta_0) = \begin{cases} \pi/2\theta_c & \text{if } \theta_0 \leqslant \theta_c \\ 0 & \text{if } \theta_0 > \theta_c \end{cases}, \tag{20}$$

where θ_c is a cutoff angle above which there are no incident phonons on the boundary. For simplicity, it is assumed that θ_c is equal for the in-plane and out-of-plane phonons.

Figure 9(a) shows the integrated transmission probabilities for the incoming LA phonons $\bar{w}_{1l\to qr}$ as a function of the cutoff angle and Fig. 9(b) shows $\bar{w}_{1t\to qr}$. The resulting value of $-C_{\mathrm{LA+TA}}/C_{\mathrm{ZA}}$ as a function of θ_c is shown in Fig. 9(c), for different drum diameters. To construct this figure, a value of $\kappa_{\mathrm{LA+TA}} = 2000$ W/m K is assumed for all the drum diameters. The most important process that alters the value of $-C_{\mathrm{LA+TA}}/C_{\mathrm{ZA}}$ is the reflection of TA phonons into ZA phonons, as this governs the temperature of the ZA phonon bath, and this can only occur at incident angles $\theta_0 \neq 0$. Therefore, at low incident angles in Fig. 9, $-C_{\mathrm{LA+TA}}/C_{\mathrm{ZA}}$ becomes very large because the ZA phonons receive no heat directly from the laser, and therefore reach a low temperature compared to the in-plane phonons. At angles above $\theta_c \approx 45$ deg, the reflection of TA phonons into ZA phonons becomes significant [Fig. 9(b)], resulting in a sharp decrease of $-C_{\mathrm{LA+TA}}/C_{\mathrm{ZA}}$ [Fig. 9(c)].

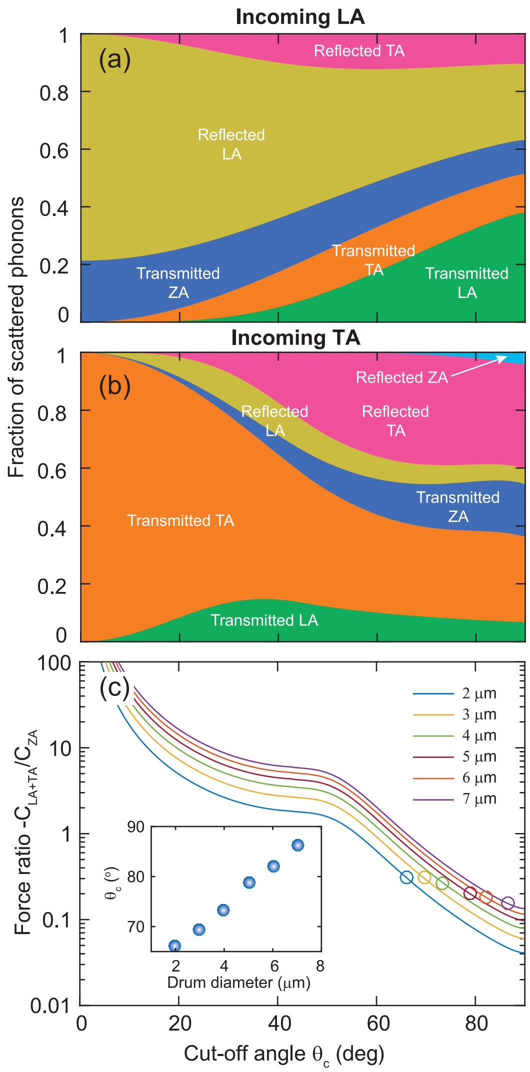

FIG. 9. Dependence on the angular distribution of the incoming phonons, assuming $\kappa_{\mathrm{LA+TA}} = 2000$ W/m K, using the model in Sec. III B with transmission coefficients adapted to the nonuniform angular phonon distribution. (a) Transmission and reflection probabilities for incoming longitudinal acoustic phonons as a function of cutoff angle θ_c for a pretension of 0.8 N/m. (b) Transmission and reflection probabilities for incoming transverse acoustic phonons as a function of cutoff angle θ_c for a pretension of 0.8 N/m. (c) Ratio $-C_{\mathrm{LA+TA}}/C_{\mathrm{ZA}}$ as a function of cutoff angle θ_c for different drum diameters. The circles represent the experimental mean from Ref. [22]. The inset shows the extracted cutoff angle θ_c based on the experimental mean values.

Using the experimental values of $-C_{\mathrm{LA+TA}}/C_{\mathrm{ZA}}$ from Ref. [22], a diameter-dependent θ_c can be extracted as shown in the inset of Fig. 9(c). Values of θ_c close to 90 deg suggest the angular distribution is close to uniform, and the LA and TA phonons are closer to the fully diffusive regime rather than the fully ballistic regime. A monotonically increasing θ_c is obtained with increasing drum size, as expected due to the increased amount of collisions experienced by the phonons as the distance between the laser spot and the boundary becomes larger, increasing the uniformity of the incoming angular phonon distribution. This scenario is therefore a reasonable explanation to the experimentally observed diameter dependence of $-C_{\mathrm{LA+TA}}/C_{\mathrm{ZA}}$.

F. Time constant of the in-plane phonons

In Ref. [22], it is argued that the thermal time constant of the in-plane phonons must be much smaller than that of the flexural phonons. Since it is complicated to solve the time dependence of the heat flow in the entire system, we estimate $\tau_{\mathrm{LA+TA}}$ using a simple model [15,48,49] based on the solution of the heat equation and by assuming the interfacial thermal resistance of the in-plane phonons to be small:

$$\tau_{\mathrm{LA+TA}} \approx \frac{a^2 \rho c_{p,\mathrm{LA+TA}}}{2\kappa_{\mathrm{LA+TA}}}. \tag{21}$$

Using the values of $\kappa_{\mathrm{LA+TA}}$ from Fig. 8, we find $\tau_{\mathrm{LA+TA}} \approx$ 2 ns. This is indeed much smaller than the observation limit in Ref. [22]. The model presented in this work thus supports the notion in Ref. [22] that $\tau_{\mathrm{LA+TA}} \ll \tau_{\mathrm{ZA}}$, because typically τ_{ZA} is found in a range between 25 and 250 ns.

IV. DISCUSSION

In future work, our model could be improved by taking into account the finite radius of the kink due to the bending rigidity of 2D materials [31,50], which will provide a more accurate picture for the reflection and transmission of phonons with short wavelengths. Furthermore, coupling to the substrate could be included as an additional pathway to transmit phonons to the heat sink. Moreover, solutions of the full Boltzmann-Peierls equation for phonon transport in graphene [51–53] can be useful to take into account the nonuniform angular distribution in a more accurate manner. Finally, the model could be improved by including the anharmonic conversion processes between in-plane acoustic phonons and flexural acoustic phonon on the suspended drum [33,34]. This provides a coupling between the phonon baths that allows heat to flow from the in-plane to out-of-plane phonon bath, while at the same time lowering $\kappa_{\mathrm{LA+TA}}$ due to the additional scattering processes, thereby improving the accuracy of the model for predicting the values of $-C_{\mathrm{LA+TA}}/C_{\mathrm{ZA}}$.

Future experiments to test our model in more detail could focus on the dependence of τ_{ZA} and $-C_{\mathrm{LA+TA}}/C_{\mathrm{ZA}}$ on the tension and the kink angle β. For example, MEMS devices could be used to strain a suspended sheet of graphene [54], which should induce significant changes in τ_{ZA}. Also inflated graphene blisters, such as studied by Bunch and Dunn [25], provide a way to introduce large changes in the kink angle β. These studies of β and strain could also shed more light on the large device-to-device variations observed in the experimental value of τ_{ZA} [15,22]. Although on larger length scales experimental techniques are available [55] to study the angular dependence of phonon transmission as in Fig. 4, these need to be scaled down further in order to be applicable for 2D materials. If this can be overcome, it would be particularly interesting to verify the transmission peak for ZA phonons that is observed near 1.1° in Fig. 4. Since Raman spectroscopy techniques to measure heat transport are mostly sensitive to the temperature of the in-plane phonon bath, they can also be useful to refine the modeling of the in-plane phonons.

V. CONCLUSION

We analyze the situation where an (optothermal) heat flux is incident at the center of a circular graphene drum. It is assumed that the heat generates only in-plane acoustic phonons, due to selective electron-phonon scattering, that propagate outward. Because of the weak interactions between in-plane and flexural phonons, only at the edge of the drum conversion between the phonon modes can occur. Here, the phonons are transmitted and reflected by a kink in graphene that is formed by sidewall adhesion. As a result of the large difference between the transmission coefficients for ZA and in-plane phonons, large differences in the acoustic phonon bath temperatures can occur. This creates a situation where the local thermal equilibrium assumption is not valid anymore on the drum. In particular, flexural phonons show a low transmission probability because their propagation speed is much lower than the in-plane phonons, which leads to a large thermal boundary resistance at the edge of the drum. This resistance results in large values of the thermal time constant τ_{ZA}, which is in line with experimental observations. Furthermore, the different phonon temperatures lead to two distinct thermal expansion forces in suspended graphene that oppose each other. The model predicts the ratio of the amplitudes of these forces in the correct order of magnitude observed in experiments and shows that size dependence of this ratio can emerge due to ballistic effects in the phonon transport.

ACKNOWLEDGMENTS

The authors thank D. R. Ladiges and J. E. Sader for fruitful discussions. This work is part of the research programme Integrated Graphene Pressure Sensors (IGPS) with Project No. 13307, which is financed by the Netherlands Organisation for Scientific Research (NWO). The research leading to these results also received funding from the European Union's Horizon 2020 research and innovation programme under Grant Agreement No. 785219 Graphene Flagship.

[1] A. K. Geim and K. S. Novoselov, The rise of graphene, Nat. Mater. **6**, 183 (2007).

[2] A. A. Balandin, S. Ghosh, W. Bao, I. Calizo, D. Teweldebrhan, F. Miao, and C. N. Lau, Superior thermal conductivity of single-layer graphene, Nano Lett. **8**, 902 (2008).

[3] D. S. Ghosh, I. Calizo, D. Teweldebrhan, E. P. Pokatilov, D. L. Nika, A. A. Balandin, W. Bao, F. Miao, and C. N. Lau, Extremely high thermal conductivity of graphene: Prospects for thermal management applications in nanoelectronic circuits, Appl. Phys. Lett. **92**, 151911 (2008).

[4] W. Cai, A. L. Moore, Y. Zhu, X. Li, S. Chen, L. Shi, and R. S. Ruoff, Thermal transport in suspended and supported monolayer graphene grown by chemical vapor deposition, Nano Lett. **10**, 1645 (2010).

[5] S. Chen, A. L. Moore, W. Cai, Ji Won Suk, J. An, C. Mishra, C. Amos, C. W. Magnuson, J. Kang, L. Shi, and R. S. Ruoff, Raman measurements of thermal transport in suspended monolayer graphene of variable sizes in vacuum and gaseous environments, ACS Nano **5**, 321 (2010).

[6] D. L. Nika and A. A. Balandin, Two-dimensional phonon transport in graphene, J. Phys.: Condens. Matter **24**, 233203 (2012).

[7] C. Faugeras, B. Faugeras, M. Orlita, M. Potemski, R. R. Nair, and A. K. Geim, Thermal conductivity of graphene in corbino membrane geometry, ACS Nano **4**, 1889 (2010).

[8] X. Xu, L. F. C. Pereira, Yu Wang, J. Wu, K. Zhang, X. Zhao, S. Bae, C. Tinh Bui, R. Xie, J. T. L. Thong, B. H. Hong, K. P. Loh, D. Donadio, B. Li, and B. Özyilmaz, Length-dependent thermal conductivity in suspended single-layer graphene, Nat. Commun. **5**, 3689 (2014).

[9] J.-U. Lee, D. Yoon, H. Kim, S. W. Lee, and H. Cheong, Thermal conductivity of suspended pristine graphene measured by Raman spectroscopy, Phys. Rev. B **83**, 081419(R) (2011).

[10] V. E. Dorgan, A. Behnam, H. J. Conley, K. I. Bolotin, and E. Pop, High-field electrical and thermal transport in suspended graphene, Nano Lett. **13**, 4581 (2013).

[11] S. Chen, Q. Li, Q. Zhang, Y. Qu, H. Ji, R. S. Ruoff, and W. Cai, Thermal conductivity measurements of suspended graphene with and without wrinkles by micro-Raman mapping, Nanotechnology **23**, 365701 (2012).

[12] J. H. Seol, I. Jo, A. L. Moore, L. Lindsay, Z. H. Aitken, M. T. Pettes, X. Li, Z. Yao, R. Huang, D. Broido, N. Mingo, R. S. Rouff, and L. Shi, Two-dimensional phonon transport in supported graphene, Science **328**, 213 (2010).

[13] S. Ghosh, W. Bao, D. L. Nika, S. Subrina, E. P. Pokatilov, C. N. Lau, and A. A. Balandin, Dimensional crossover of thermal transport in few-layer graphene, Nat. Mater. **9**, 555 (2010).

[14] E. Pop, V. Varshney, and A. K. Roy, Thermal properties of graphene: Fundamentals and applications, MRS Bull. **37**, 1273 (2012).

[15] R. J. Dolleman, S. Houri, D. Davidovikj, S. J. Cartamil-Bueno, Y. M. Blanter, H. S. J. van der Zant, and P. G. Steeneken, Optomechanics for thermal characterization of suspended graphene, Phys. Rev. B **96**, 165421 (2017).

[16] K. Azizi, P. Hirvonen, Z. Fan, A. Harju, K. R. Elder, T. Ala-Nissila, and S. M. V. Allaei, Kapitza thermal resistance across individual grain boundaries in graphene, Carbon **125**, 384 (2017).

[17] A. Cao and J. Qu, Kapitza conductance of symmetric tilt grain boundaries in graphene, J. Appl. Phys. **111**, 053529 (2012).

[18] Q.-X. Pei, Y.-W. Zhang, Z.-D. Sha, and V. B. Shenoy, Carbon isotope doping induced interfacial thermal resistance and thermal rectification in graphene, Appl. Phys. Lett. **100**, 101901 (2012).

[19] W. Xu, G. Zhang, and B. Li, Interfacial thermal resistance and thermal rectification between suspended and encased single layer graphene, J. Appl. Phys. **116**, 134303 (2014).

[20] H. Sevinçli and M. Brandbyge, Phonon scattering in graphene over substrate steps, Appl. Phys. Lett. **105**, 153108 (2014).

[21] M. M. Rojo, Z. Li, C. Sievers, A. C. Bornstein, E. Yalon, S. Deshmukh, S. Vaziri, M.-Ho Bae, F. Xiong, D. Donadio, and

E. Pop, Thermal transport across graphene step junctions, 2D Mater. **6**, 011005 (2018).

[22] R. J. Dolleman, G. J. Verbiest, Y. M. Blanter, H. S. J. van der Zant, and P. G. Steeneken, Nonequilibrium thermodynamics of acoustic phonons in suspended graphene, Phys. Rev. Research **2**, 012058 (2020).

[23] J. S. Bunch, S. S. Verbridge, J. S. Alden, A. M. van der Zande, J. M. Parpia, H. G. Craighead, and P. L. McEuen, Impermeable atomic membranes from graphene sheets, Nano Lett. **8**, 2458 (2008).

[24] Z. Lu and M. L. Dunn, van der Waals adhesion of graphene membranes, J. Appl. Phys. **107**, 044301 (2010).

[25] J. S. Bunch and M. L. Dunn, Adhesion mechanics of graphene membranes, Solid State Commun. **152**, 1359 (2012).

[26] Herbert Kolsky, *Stress Waves in Solids* (Dover, New York, 1963) (unabridged and corrected republication).

[27] See Supplemental Material at http://link.aps.org/supplemental/10.1103/PhysRevB.101.115411 for the full expressions of the continuity of deflection and stress, calculations of the thermal interface resistance in the case of local thermal equilibrium, and the full solutions for the internal energies in the two-temperature model.

[28] R. E. Peterson and A. C. Anderson, The Kapitza thermal boundary resistance, J. Low Temp. Phys. **11**, 639 (1973).

[29] J. Atalaya, A. Isacsson, and J. M. Kinaret, Continuum elastic modeling of graphene resonators, Nano Lett. **8**, 4196 (2008).

[30] L. E. Kinsler, A. R. Frey, A. B. Coppens, and J. V. Sanders, *Fundamentals of Acoustics* (John Wiley & Sons, New York 2000).

[31] R. Ghaffari and R. A. Sauer, Modal analysis of graphene-based structures for large deformations, contact, and material nonlinearities, J. Sound Vib. **423**, 161 (2018).

[32] D. Singh, J. Y. Murthy, and T. S. Fisher, Spectral phonon conduction and dominant scattering pathways in graphene, J. Appl. Phys. **110**, 094312 (2011).

[33] A. K. Vallabhaneni, D. Singh, H. Bao, J. Murthy, and X. Ruan, Reliability of Raman measurements of thermal conductivity of single-layer graphene due to selective electron-phonon coupling: A first-principles study, Phys. Rev. B **93**, 125432 (2016).

[34] L. Lindsay, D. A. Broido, and N. Mingo, Flexural phonons and thermal transport in graphene, Phys. Rev. B **82**, 115427 (2010).

[35] C. Lee, X. Wei, J. W. Kysar, and J. Hone, Measurement of the elastic properties and intrinsic strength of monolayer graphene, Science **321**, 385 (2008).

[36] R. J. Dolleman, S. Houri, A. Chandrashekar, F. Alijani, H. S. J. van der Zant, and P. G. Steeneken, Opto-thermally excited multimode parametric resonance in graphene membranes, Sci. Rep. **8**, 9366 (2018).

[37] X.-J. Ge, K.-L. Yao, and J.-T. Lü, Comparative study of phonon spectrum and thermal expansion of graphene, silicene, germanene, and blue phosphorene, Phys. Rev. B **94**, 165433 (2016).

[38] D. L. Nika, S. Ghosh, E. P. Pokatilov, and A. A. Balandin, Lattice thermal conductivity of graphene flakes: Comparison with bulk graphite, Appl. Phys. Lett. **94**, 203103 (2009).

[39] N. Mounet and N. Marzari, First-principles determination of the structural, vibrational, and thermodynamic properties of diamond, graphite, and derivatives, Phys. Rev. B **71**, 205214 (2005).

[40] P. K. Schelling and P. Keblinski, Thermal expansion of carbon structures, Phys. Rev. B **68**, 035425 (2003).

[41] S. Mann, R. Kumar, and V. K. Jindal, Negative thermal expansion of pure and doped graphene, RSC Adv. **7**, 22378 (2017).

[42] P. G. Klemens and D. F. Pedraza, Thermal conductivity of graphite in the basal plane, Carbon **32**, 735 (1994).

[43] S. Lee, D. Broido, K. Esfarjani, and G. Chen, Hydrodynamic phonon transport in suspended graphene, Nat. Commun. **6**, 6290 (2015).

[44] A. Cepellotti, G. Fugallo, L. Paulatto, M. Lazzeri, F. Mauri, and N. Marzari, Phonon hydrodynamics in two-dimensional materials, Nat. Commun. **6**, 6400 (2015).

[45] X. Gu and R. Yang, First-principles prediction of phononic thermal conductivity of silicene: A comparison with graphene, J. Appl. Phys. **117**, 025102 (2015).

[46] X. Gu, Y. Wei, X. Yin, B. Li, and R. Yang, Colloquium: Phononic thermal properties of two-dimensional materials, Rev. Mod. Phys. **90**, 041002 (2018).

[47] S. Lepri, R. Livi, and A. Politi, Thermal conduction in classical low-dimensional lattices, Phys. Rep. **377**, 1 (2003).

[48] K. L. Aubin, Radio frequency nano/microelectromechanical resonators: Thermal and nonlinear dynamics studies, Ph.D. thesis, Cornell University, Ithaca, NY, 2004.

[49] J. S. Bunch, Mechanical and electrical properties of graphene sheets, Ph.D. thesis, Cornell University, Ithaca, NY, 2008.

[50] N. Lindahl, D. Midtvedt, J. Svensson, O. A. Nerushev, N. Lindvall, A. Isacsson, and E. E. B. Campbell, Determination of the bending rigidity of graphene via electrostatic actuation of buckled membranes, Nano Lett. **12**, 3526 (2012).

[51] J.-P. M. Péraud, C. D. Landon, and N. G. Hadjiconstantinou, Monte Carlo methods for solving the Boltzmann transport equation, Ann. Rev. Heat Trans. **17**, 205 (2014).

[52] L. Lindsay, W. Li, J. Carrete, N. Mingo, D. A. Broido, and T. L. Reinecke, Phonon thermal transport in strained and unstrained graphene from first principles, Phys. Rev. B **89**, 155426 (2014).

[53] C. D. Landon and N. G. Hadjiconstantinou, Deviational simulation of phonon transport in graphene ribbons with *ab initio* scattering, J. Appl. Phys. **116**, 163502 (2014).

[54] M. Goldsche, G. J. Verbiest, T. Khodkov, J. Sonntag, N. von den Driesch, D. Buca, and C. Stampfer, Fabrication of comb-drive actuators for straining nanostructured suspended graphene, Nanotechnology **29**, 375301 (2018).

[55] J. P. Wolfe, *Imaging Phonons: Acoustic Wave Propagation in Solids* (Cambridge University Press, New York, 2005).